Rock Mechanics and Rock Engineering (2020) 53:5239–5255
https://doi.org/10.1007/s00603-020-02214-z

ORIGINAL PAPER

The Microscopic Mechanism of Crack Evolution in Brittle Material Containing 3-D Embedded Flaw

Bangxiang Li[1,3] · Song Yu[2] · Weishen Zhu[1] · Weibing Cai[1,3] · Lei Yang[1,2] · Yiguo Xue[1,2] · Yong Li[1,3]

Received: 6 February 2020 / Accepted: 22 July 2020 / Published online: 7 August 2020

Abstract
In this paper, the microscopic mechanism of crack evolution in brittle material containing 3-D embedded flaw is investigated. The crack evolution mode of 3-D flaw is summarized by the uniaxial compression experiment first. Based on experiment results, the micro-parameters in the flat-joint model are calibrated and numerical models containing 3-D embedded flaw are established in PFC3D. Then, the numerical uniaxial compression experiment is carried out to validate the effectiveness of numerical model. The simulation results indicate that the flat-joint model is appropriate to model the cracking processes of 3-D flaw. The method of particle velocity vector field is introduced to analyze crack evolution mechanism, and four types of particle velocity vector field corresponding to typical cracks are proposed. Generally, the initiation of wing crack is tensile crack and the further propagation is mixed tensile and shear crack. However, the interaction between flaws has important impacts on the crack evolution mechanism and the specimen failure mode. In the rock bridge, wing crack may initiate as mixed tensile and shear crack. The failure mode turns from burst failure to splitting failure with the condition changing from single flaw to double flaws.

Keywords 3-D crack · Flat-joint model (FJM) · Microscopic mechanism · Particle velocity field · Interaction between flaws

1 Introduction

Rock is a brittle material that contains many pre-existing discontinuities such as bedding planes, joints, flaws, and pores. Pre-existing discontinuity plays an important role in governing the mechanical and failure behavior of brittle rock. New cracks initiate at or near the tips of pre-existing discontinuities, propagate and coalesce, leading to the damage and even failure of rocks.

Extensive research has been done on crack propagation and coalescence from 2-D pre-existing flaws (Shen et al. 1995; Bobet and Einstein 1998a; Wong and Chau 1998; Park and Bobet 2010; Yang and Jing 2010; Lee and Jeon 2011; Zhuang et al. 2014; Cao et al. 2015; Cheng et al. 2016). However, the CT tomography shows that the pre-existing discontinuities in rocks are usually three-dimensional rather than two-dimensional (Bubeck et al. 2017). Investigating crack evolution mode from 3-D pre-existing flaws is more suitable for engineering practice.

Adams and Sines (1978) summarized crack types initiating from a 3-D pre-existing embedded flaw. Dyskin et al. (1994a, b), Sahouryeh et al. (2002) and Wang et al. (2019) conducted a series of uniaxial and biaxial compression experiments on specimens containing single 3-D pre-existing flaw. For 3-D flaw, the crack initiation and propagation mode was quite different from that in 2-D cases. Wing crack wrapped around the 3-D flaw and could only propagate to about the size of the flaw. Therefore, the single 3-D pre-existing flaw was insufficient to cause specimen failure directly (Germanovich and Dyskin 2000).

To investigate the impact of interaction between pre-existing flaws on crack evolution, Dyskin et al. (2003) and Fu et al. (2013) conducted uniaxial compression experiments on specimens containing two 3-D embedded pre-existing flaws. Experiment results demonstrated that crack propagation

✉ Song Yu
yusong@sdu.edu.cn

✉ Yong Li
yongli@sdu.edu.cn

1 Geotechnical and Structural Engineering Research Center, Shandong University, Jinan 250061, China

2 School of Civil Engineering, Shandong University, Jinan 250061, China

3 School of Qilu Transportation, Shandong University, Jinan 250002, China

was very sensitive to the spacing between flaws. When the flaws are close enough, the interaction between flaws could amplify the propagation of wing cracks significantly and caused specimen splitting failure. Zhou et al. (2018) investigated the cracking behavior of two 3D cross-embedded flaws and found the ultimate failure of specimen was induced by the further propagation of wing crack. Besides, some studies focused on the 3-D surface flaw (Wong et al. 2004a, b, 2006, 2007; Yin et al. 2014). The results showed with flaw penetration depth increasing, the crack propagation mode transformed gradually from 3-D to 2-D.

Based on laboratory experiment results, the mechanism of crack evolution was investigated by different numerical methods, including finite element method (Bocca et al. 1990; Xu and Fowell 1994), extended finite element method (Budyn et al. 2004; Zhou et al. 2010), displacement discontinuity method (Bobet 2000; Bobet and Einstein 1998b), and boundary element method (Hosseini-Tehrani et al. 2005; Lu and Wu 2006). It should be noted that it is crucial to choose proper fracture criteria when simulating by these methods.

With reference to previous research results (Zhang and Wong 2012), the complex empirical constitutive behavior can be replaced by simple particle contact model. The standard bonded-particle model (BPM) (Potyondy and Cundall 1996, 2004) based on Particle Flow Code (PFC) has been widely used in 2-D fractured rock damage analysis (Lee and Jeon 2011; Zhang and Wong 2012, 2013; Manouchehrian and Marji 2012; Manouchehrian et al. 2014; Ghazvinian et al. 2012; Sarfarazi et al. 2014; Yang et al. 2014; Zhang et al. 2015; Cao et al. 2016). Zhang and Wong (2012, 2013, 2014) and Zhang et al. (2015) introduced the methods of displacement trend lines and force vector field to analyze crack evolution mechanisms of 2-D pre-existing flaws. Yang et al. (2014) and Yang and Huang (2018) investigated the crack evolution mechanism of two unparalleled flaws based on particle displacement and stress fields and statistics of tensile and shear crack quantity.

However, in 3-D fractured rock damage simulating, some intrinsic problems are associated with the standard BPM, such as lower model brittleness and internal friction angle (Wu and Xu 2016), causing simulating results inconsistent with experiment phenomena. For these reasons, Potyondy (2012a, b, 2013) proposed a new bond model: flat-joint model (FJM). This model has been validated by a few research through a strict comparison between 3-D simulations and laboratory experiments such as the uniaxial compression test (Bahaaddini et al. 2019), direct shear test (Yang and Qiao 2018), and Brazilian test (Xu et al. 2016).

The previous researches paid more attention to crack evolution from 2-D flaw but less attention on the 3-D embedded flaw. Moreover, the microscopic mechanism of 3-D crack propagation is rarely investigated. Therefore, it is necessary to conduct the fracture experiment and simulation on brittle material containing 3-D embedded flaw.

In this research, the crack evolution mode of 3-D embedded flaw is first summarized by uniaxial compression experiment. Based on experiment results, a set of micro-parameters in FJM are calibrated and numerical model containing 3-D embedded flaw is built in PFC3D. Then, the numerical uniaxial compression experiment is carried out to validate the effectiveness of numerical model. Finally, the microscopic mechanisms of crack evolution are analyzed and the impacts of interaction between flaws on crack evolution are investigated. The term flaw refers to those pre-existing artificial crack, and the term *crack* refers to new fracture initiating at or near the tips of flaws.

2 The Fracture Experiment of 3-D Flaw

2.1 Specimen Preparation and Experimental Equipment

To observe the cracking process of 3-D embedded flaw directly, one type of transparent rock-like resin (Li et al. 2019) is adopted to manufacture specimen in this research. The brittleness (ratio of uniaxial compression strength to tensile strength) of the resin can reach 9.98 at −45 °C, which is close to some typical rocks such as marble and sandstone, and the transparency is excellent.

Two types of specimens with single flaw and double flaws are manufactured. The size of the specimen is 70 × 70 × 140 mm. The 3-D flaw is preset in the center of the specimen. The flaw shape is an ellipse whose size is 20 × 15 mm (major axis × minor axis) and thickness is 1.8 mm. The flaw dip angle is 45° for the single-flaw condition and 30° for the double-flaw condition. In double-flaw condition, flaws are arranged parallelly. The projections of flaw in vertical direction overlap. The spacing of rock bridge *S* which is the vertical distance from the lower tip of upper flaw to the upper tip of lower flaw is 10 mm. During compression, the flaw surfaces will not contact. Therefore, the flaw can be regarded as an open flaw. The sizes and structures of the specimen and 3-D flaw are shown in Fig. 1

Uniaxial compression load is applied by electro-hydraulic servo testing machine. The testing machine is equipped with an ultra-low temperature environment box to maintain the temperature of the testing area at −45 °C stably, avoiding the influence of temperature rising on specimen brittleness. During the experiment, the crack evolution process is monitored by a digital camera. The initiation of crack is identified by visual inspection. The experimental equipment is shown in Fig. 1.

2.2 The Crack Evolution Mode of the 3-D Single Flaw

The crack evolution mode of the 3-D single flaw is shown in Fig. 2. Several small cracks first initiate at the lower tip

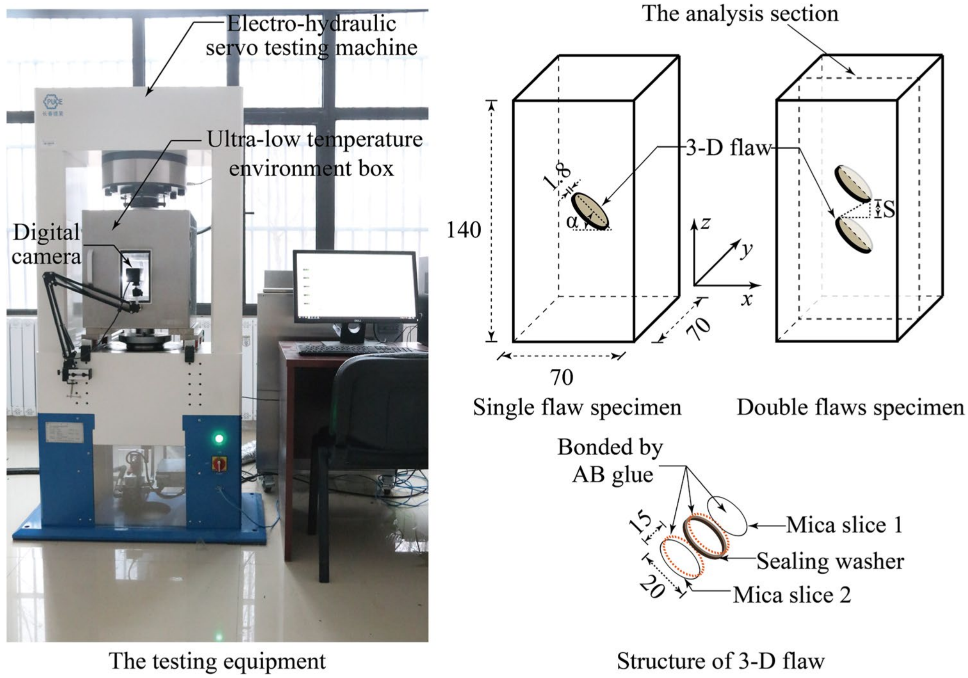

Fig. 1 The testing equipment and specimen geometries (units: mm)

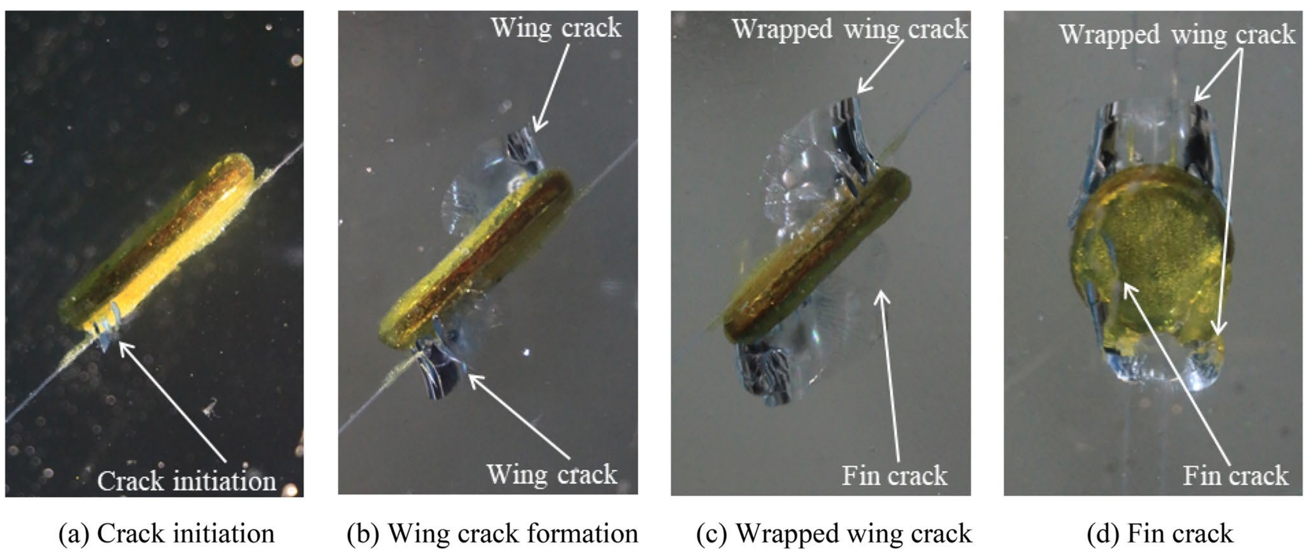

Fig. 2 The crack evolution mode of the 3-D single flaw

of the flaw (Fig. 2a) when the axial load σ_i reaches about 33% σ_c (σ_c is the peak strength of the specimen). These small cracks merge with each other, forming wing cracks at the tips of the flaw (Fig. 2b). With σ_i increasing, wing cracks propagate stably and form wrapped wing cracks (Fig. 2c). During the stable propagation of wing cracks, fin cracks initiate on the upper and lower surfaces of the 3-D flaw (Fig. 2d).

In this condition, the propagation of wing crack stops after reaching an ultimate propagation length and is insufficient to cause specimen failure directly. When σ_i approaches σ_c, a mass of cracks are generated instantaneously, leading to specimen burst failure and losing integrality.

2.3 The Crack Evolution Mode of 3-D Double Flaws

Figure 3 is the crack evolution mode of 3-D double flaws. When σ_i reaches about 29% σ_c, wing cracks first initiate inside the rock bridge (Fig. 3a). These two wing cracks propagate toward the tips of their opposite flaw which isolates the center of rock bridge to form a core (Fig. 3b). When

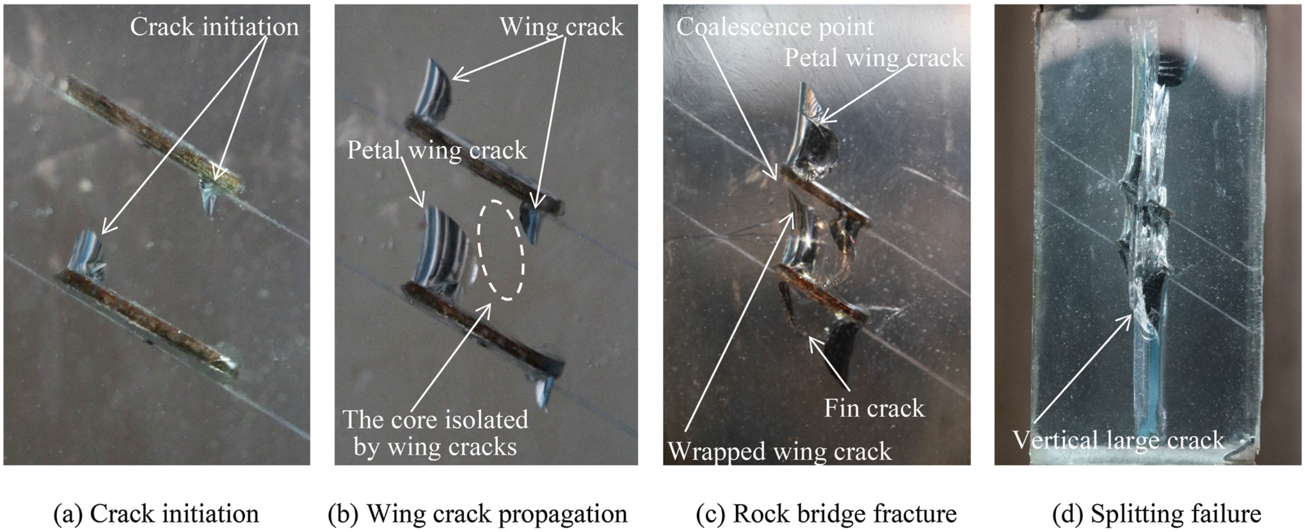

Fig. 3 The crack evolution mode of 3-D double flaws

σ_i reaches about 79% σ_c, the left wing crack propagates to the upper tip of the upper flaw, which indicates the fracture of rock bridge (Fig. 3c). After that, the wing cracks link to each other and coalesce into a vertical large crack, inducing splitting failure of the specimen (Fig. 3d).

2.4 The Impacts of Interaction Between 3-D Flaws on Crack Evolution Mode

The interaction between flaws significantly promotes the propagation of wing crack. In single flaw condition, the propagation of wing crack exists ultimate length which is consistent with the "self-limiting" effect proposed by Dyskin et al. (1994a, b, 2003), while in double-flaw condition, wing cracks propagate continually.

According to the sizes adopted in this research, the flaw is relatively small compared with the specimen. The weakening effect of the flaw on the specimen is confined to the region surrounding the flaw. It is similar to the local effect of the "Saint–Venant principle". In the single-flaw condition, wing crack can only propagate within the weakened zone. However, in the double 3-D flaws condition, the weakened zone is significantly enlarged by the interaction between flaws. After rock bridge fracture, the weakened zone is further enlarged to the entire specimen. Hence, the wing crack can propagate continuously.

The promotion of the interaction between flaws in crack evolution changes the specimen failure mode. In the single flaw condition, the propagation of wing crack is insufficient to cause specimen failure directly and the failure mode is burst failure. In the double-flaw condition, the continuous propagation of wing crack induces specimen splitting failure.

3 Numerical Simulation

3.1 Numerical Model Based on FJM in PFC3D

In the simulation of PFC3D, the material is dispersed into bonded spherical rigid particles. The mechanical behavior of the material is simulated by particle motion, interaction, and bond breakage.

In the flat-joint model (FJM), the contact surface between particles is discretized into elements, with each element being either bonded or unbonded. When the stress of certain element exceeds the tensile or shear strength of contact, this element breaks contributing partial damage to the contact. When all elements break, the flat-joint contact is completely damaged.

The numerical model based on FJM is shown in Fig. 4. To reproduce the relevant mechanical behavior of rock-like resin, microscopic parameters need to be calibrated with macroscopic mechanical parameters obtained in laboratory experiments. Table 1 is the parameter comparison between numerical model and rock-like resin.

During the calibration process, the microscopic parameters are confirmed by using the trial and error method. Although the understanding of this calibration process is still incomplete, some connection can be established between the microscopic and macroscopic parameters. The macroscopic Young's modulus is proportional to the stiffness of particle and FJM. The Poisson's ratio is proportional to stiffness ratio. The uniaxial compressive strength is mainly controlled by the tensile and shear strength of the FJM ($\bar{\sigma}_c$ and $\bar{\tau}_c$). The shear strength $\bar{\tau}_c$ follows the Coulomb criterion and is determined by the cohesion C and friction angle ϕ of the FJM. The ratio of tensile strength to shear strength ($\bar{\sigma}_c/\bar{\tau}_c$) is a key

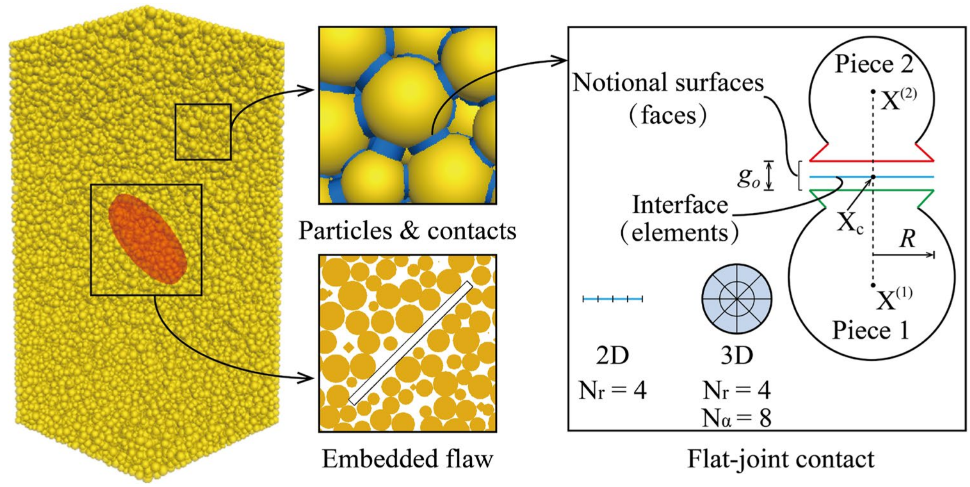

Fig. 4 Numerical model and flat-joint contact

Table 1 Parameter comparison between rock-like resin and numerical model

	Rock-like resin	Flat-joint model
Density, ρ(g/cm^3)	1.43	1.43
Young's modulus, E(GPa)	5.15	5.20
Poisson's ratio	0.25	0.22
Uniaxial compressive strength, UCS(MPa)	121.31	119.79

parameter which is related to the breakage type and specimen failure mode. Table 2 lists the calibrated microscopic parameters in the FJM model.

Numerical specimens are established according to the specimen and flaw geometries in the laboratory experiment. An elliptic cylinder geometry is pre-imported and named flaw group, a wall is also created by importing this geometry. Particles are randomly distributed within the range of specimen sizes except for the flaw group. During the cycle to calm the particle assembly, the wall blocks particles from moving into the flaw group. After the particle assembly reaches equilibrium, the wall is deleted and the 3-D open flaw is created. It should be noted that due to the randomly generated particle positions and radii, the flaw has some shape and size errors and its surfaces are rough. The flaw surface will not contact during compression, therefore the rough surfaces have no significant effect on crack initiation and propagation.

3.2 The Validation of Numerical Model

To validate the effectiveness of numerical model on simulating the cracking process of 3-D flaw, the numerical specimens are loaded by uniaxial compression in a displacement controlled manner. Tables 3 and 4 are the crack evolution modes of the 3-D single and double flaws in numerical simulation. The blue elliptic geometry and spot in the picture are 3-D flaw and broken bond respectively. Bond break indicates micro-crack initiation, and the concentration of breaks in one region denotes the formation of macro-crack. Both the cracking processes of single flaw and double flaws are divided into three stages.

In simulation, the propagation of wing crack in single flaw condition also exists the ultimate propagation length (Table 3i). The failure mode in double flaws condition is splitting failure (Table 4i). By comparing Figs. 2, 3 and Tables 3, 4, it can be observed that the crack evolution modes in the numerical simulation are consistent with those in the laboratory experiment,

Table 2 The microscopic parameters in the FJM model

Flat-Joint model parameters		Particle parameters	
Particle and contact modulus, E^* (GPa)	4.8	Minimum particle diameter, R_{min}(mm)	1
Stiffness ratio of the particle and contact, k_n/k_s	4.5	Maximum to minimum particle diameter ratio, R_{max}/R_{min}	1.8
Tensile strength of the contact, $\bar{\sigma}_c$(MPa)	40.1	Radius multiplier, $\bar{\lambda}$	1.0
Cohesion of the contact, C (MPa)	32.1	Residual friction coefficient, μ	0.1
Friction angle of the contact, ϕ (°)	30	Particle density, ρ (g/cm^3)	1.8
Number of element in radial direction, N_r	4		
Number of element in circumferential direction, N_α	8		

Table 3 Crack initiation and propagation modes of the 3-D single flaw in simulation

<table>
<tr><td>Crack initiation stage (33%σc~49%σc)</td><td>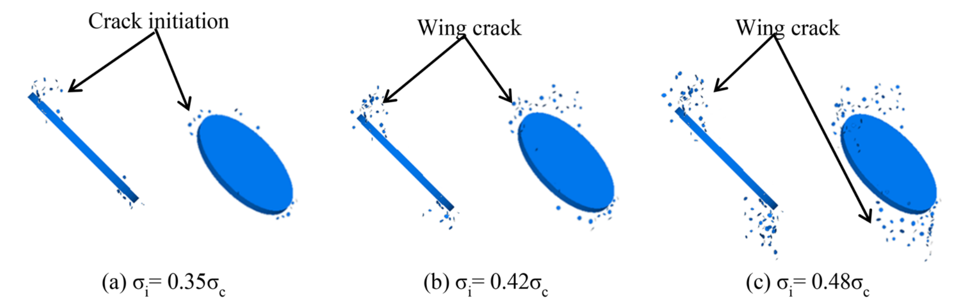

(a) $\sigma_i = 0.35\sigma_c$ (b) $\sigma_i = 0.42\sigma_c$ (c) $\sigma_i = 0.48\sigma_c$</td></tr>
<tr><td>Crack stable propagation stage (49%σc~72%σc)</td><td>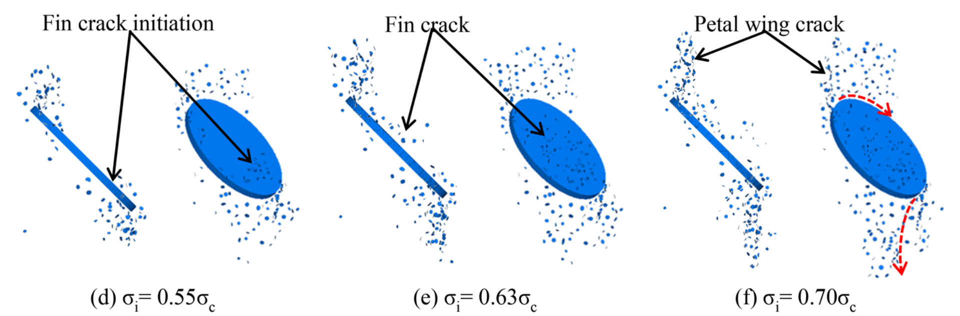

(d) $\sigma_i = 0.55\sigma_c$ (e) $\sigma_i = 0.63\sigma_c$ (f) $\sigma_i = 0.70\sigma_c$</td></tr>
<tr><td>Crack ultimate propagation stage (72%σc~89%σc)</td><td>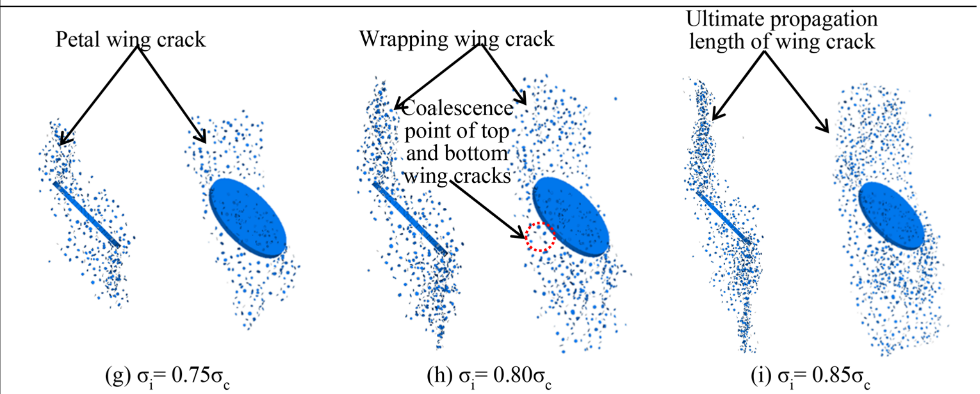

(g) $\sigma_i = 0.75\sigma_c$ (h) $\sigma_i = 0.80\sigma_c$ (i) $\sigma_i = 0.85\sigma_c$</td></tr>
</table>

indicating the numerical model based on FJM can accurately simulate the cracking processes of 3-D flaw.

4 The Microscopic Mechanism of Crack Evolution

To investigate the crack evolution mechanism of the 3-D flaw, the vertical plane (x–z plane) where the major axis of 3-D flaw is located ($y = 0.035$ mm) is chosen as the analysis section, as shown in Fig. 1. The types of breakage that constitutes wing crack and the particle velocity vector field on this section are analyzed.

It should be noted that the particles are 3-D spheres and the particle velocities are 3-D vectors. For display purposes, the particles and the vectors intersecting with the section are projected to the section plane. The size of particle profile on the section will change with particle motioning, and the vectors are displayed in 2-D form.

4.1 The Particle Velocity Trend Lines Method

In PFC3D, the discrete particles cannot produce a continuous stress and strain fields. The analysis method in fracture mechanics is unsuited for application. To analyze crack nature, Zhang and Wong (2014) introduced a displacement vector trend line method. However, the displacement vector is often lagging to reflect the cracking mechanism. In this research, the particle velocity vector is adopted instead of the displacement vector. Four types of velocity vector field corresponding to typical cracks are summarized and named type I, II, III, IV, respectively, as shown in Fig. 5.

Type I and III represent tensile crack. In type I, the particle velocity vectors distribute symmetrically and diverge from each other, forming a tensile region in the middle area.

Table 4 Crack evolution mode of 3-D double flaws in simulation

Crack initiation stage ($27\%\sigma_c$~$52\%\sigma_c$)	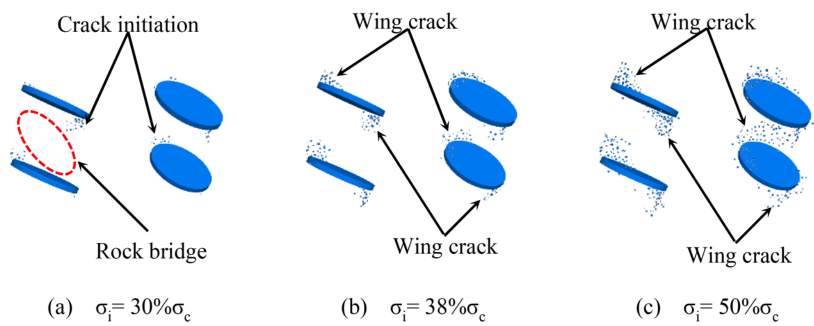
Crack propagation and coalescence stage ($52\%\sigma_c$~$80\%\sigma_c$)	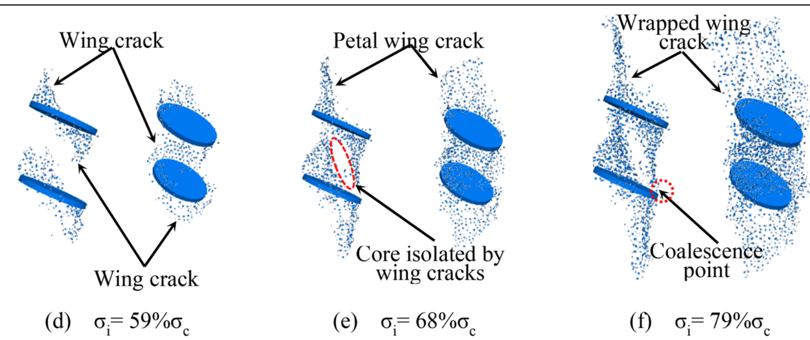
Crack unstable propagation stage ($80\%\sigma_c$~$100\%\sigma_c$)	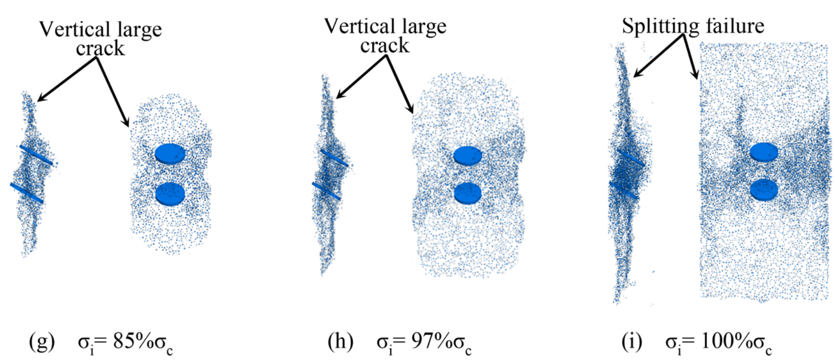

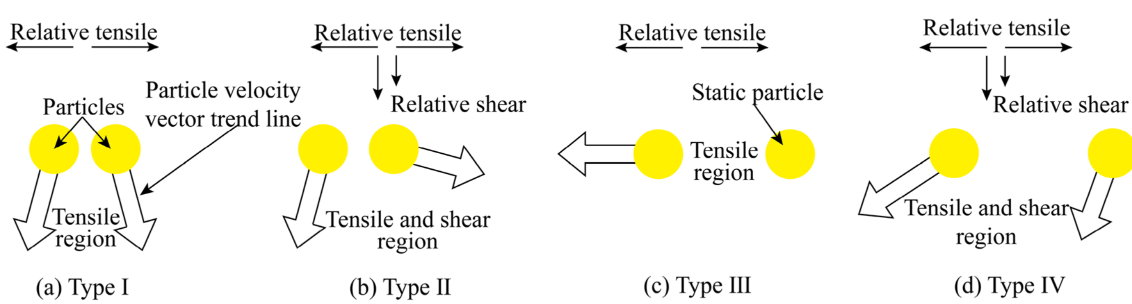

Fig. 5 Four types of velocity vector field corresponding to typical cracks

In type III, particle in one side is static, while the other side motions away from the static particle, also forming tensile region in the middle area. Types II and IV represent mixed tensile and shear crack. In type II, the particle velocity vectors distribute asymmetrically, forming mixed tensile and shear region in the middle area. In type IV, the horizontal and vertical component modules on one side are greater than those on the other side, also forming mixed tensile and shear region in the middle area. In this research, types I and II are the most common velocity vector field, and types III and IV are observed only in rock bridge.

4.2 3-D Single-Flaw Condition

Figure 6 shows the types of breakage on the section corresponding to different stresses in Table 3. The yellow dot denotes tensile breakage and the red dot denotes shear breakage. When wing crack initiates, it is composed of tensile breakages (Fig. 6a). During the stable propagation of wing crack, shear breakages are generated gradually (Fig. 6b, c). When wing crack gets into unstable propagation, the quantity of shear breakage rapidly increases (Fig. 6d). While in the later period of ultimate propagation, there are only a few tensile breakages and basically no shear breakage initiating, the propagation of wing crack reaches ultimate length and stops (Fig. 6e).

Figure 7, which corresponds to Fig. 6a and c, represents the particle velocity vector fields on the section during the initiation and propagation of wing crack. In Fig. 7a, the velocity vector field is divided into two parts bounded by flaw tip: the left part of velocity vectors turns to the bottom left, while the right part turns to the bottom right. The two parts are symmetrically distributed, which coincides with type I. The initiation of wing crack is tensile crack. In Fig. 7b, the particle velocity vector field presents obvious asymmetric characteristics: the modules of the left part of velocity vector are greater than those of the right part. This asymmetric distribution coincides with type II. Hence, the propagation of wing crack is mixed tensile and shear crack.

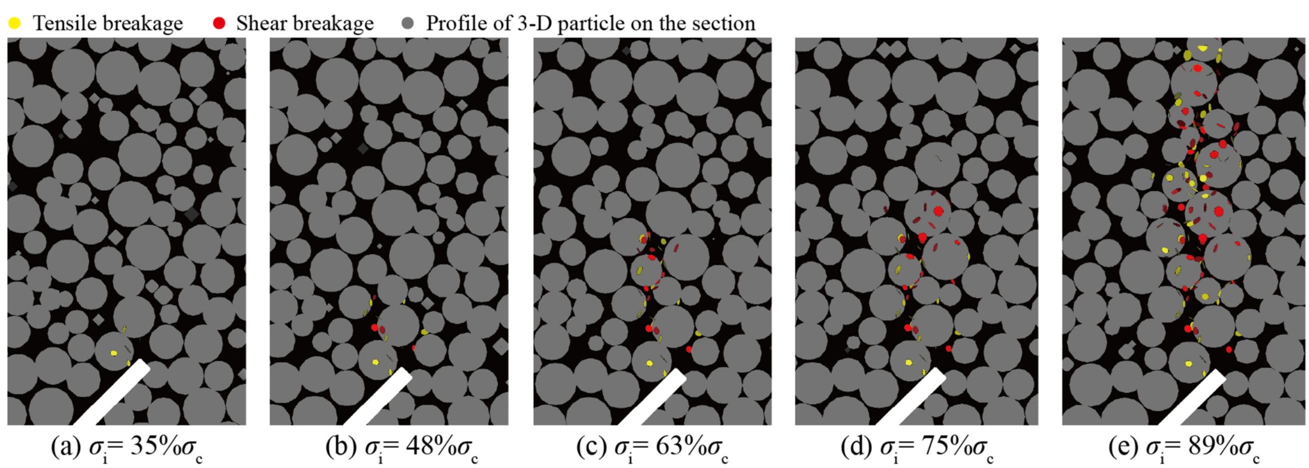

Fig. 6 The types of breakage on the section corresponding to different stresses

Fig. 7 The particle velocity vector field on the section during the initiation and propagation of wing crack

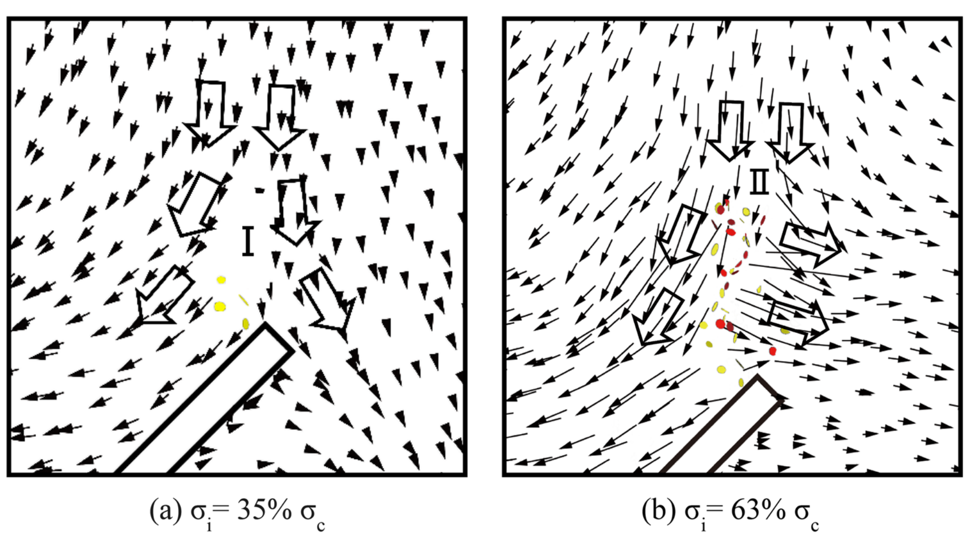

Figure 8 is the particle velocity vector field on the section before wing crack propagates to the ultimate length, corresponding to Fig. 6e. At this moment, the velocity vector field recovers to a symmetrical distribution again. Especially at the top of the wing crack, only tensile effect exists. Wing crack ceases to propagate and reaches the ultimate length.

The asymmetrical characteristic of the particle velocity vector field is gradually weakened with wing crack propagating (Fig. 7) and finally vanishes (Fig. 8). With wing crack connecting with the interior space of flaw, the shear stiffness of the wing crack surface reduces greatly, promoting the left part of particles deforming to the interior space and inducing relatively large vertical velocity, while the right part of particle motion move more laterally. Hence, the distribution of particle velocity vectors is asymmetrical. With the further propagation of wing crack, the weakening effect on shear stiffness reduces constantly. Therefore, in the crack ultimate propagation stage, the velocity vector field recovers to a symmetrical distribution.

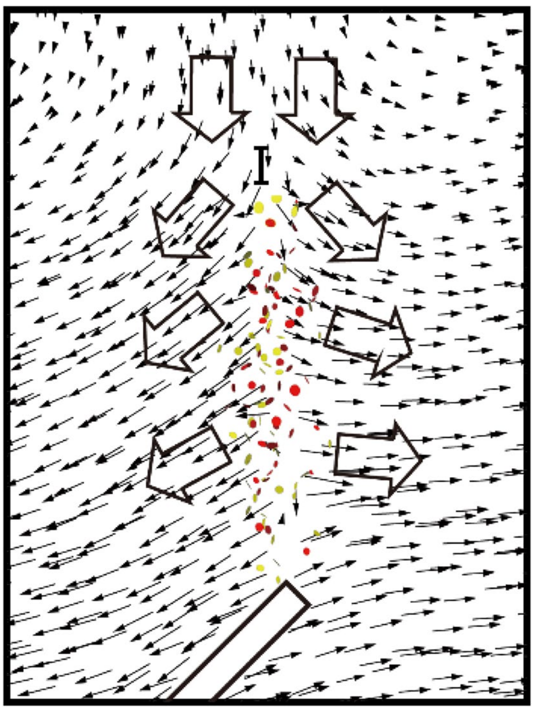

Fig. 8 The particle velocity vector field on the section before wing crack propagates to the ultimate length

4.3 3-D Double-Flaw Condition

The section in this condition is divided into two parts: the part outside the rock bridge and that inside the rock bridge.

4.3.1 The Part Outside the Rock Bridge

Figure 9 shows the types of breakage outside the rock bridge on the section corresponding to different stresses in Table 4. The breakage types during crack initiation and stable propagation are similar to those in single flaw condition, as shown in Fig. 9a–d. However, when vertical large crack is formed, the tensile breakage increases rapidly, inducing specimen splitting failure (Fig. 9e).

Figure 10 which corresponds to Fig. 9a and b shows the particle velocity vector field outside the rock bridge during the initiation and stable propagation of wing crack. The initiation of wing crack is tensile crack and the propagation is mixed tensile and shear crack which are similar to single flaw condition.

Figure 11 shows the particle velocity vector field outside the rock bridge before splitting failure, corresponding to Fig. 9e. At this moment, the velocity vector field returns to a symmetrical distribution which coincides with type I. Under the tensile effect, the fracture surface is parallel to the direction of the axial load and splits the specimen.

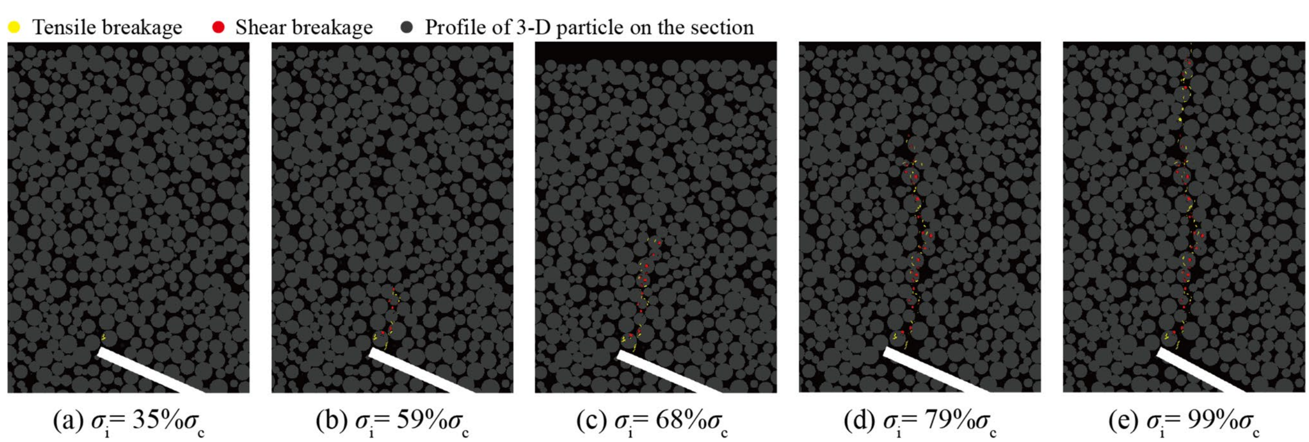

Fig. 9 The types of breakages outside the rock bridge on the section corresponding to different stresses

Fig. 10 The particle velocity vector field outside the rock bridge during the initiation and propagation of wing crack

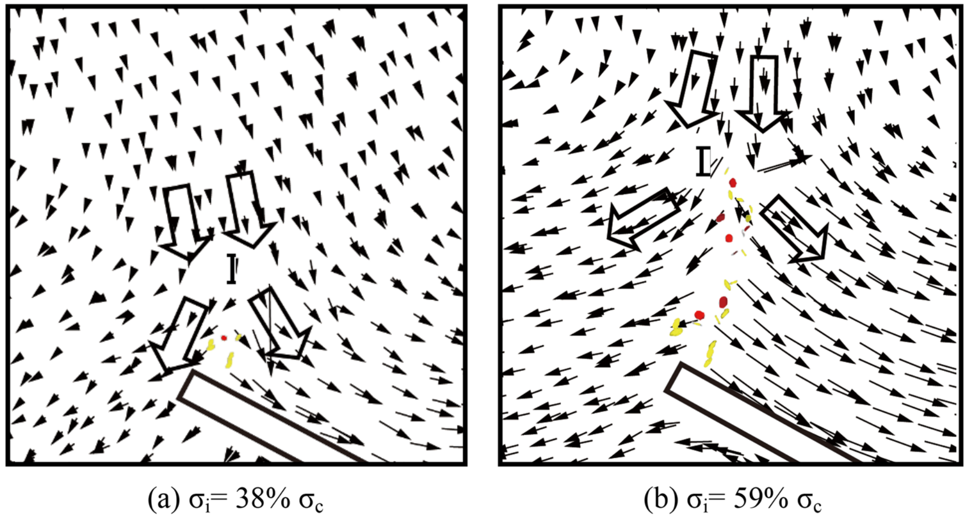

4.3.2 The Part Inside Rock Bridge

Figure 12 shows the types of breakage inside the rock bridge on the section corresponding to different stresses and the cracks are numbered. The breakage types of wing crack 1 and 2 at initiation are different: the type are shear breakages in wing crack 1 and almost tensile breakages in wing crack 2 (Fig. 12a). With further propagation, both wing cracks 1 and 2 contain tensile and shear breakages (Fig. 12b, c).

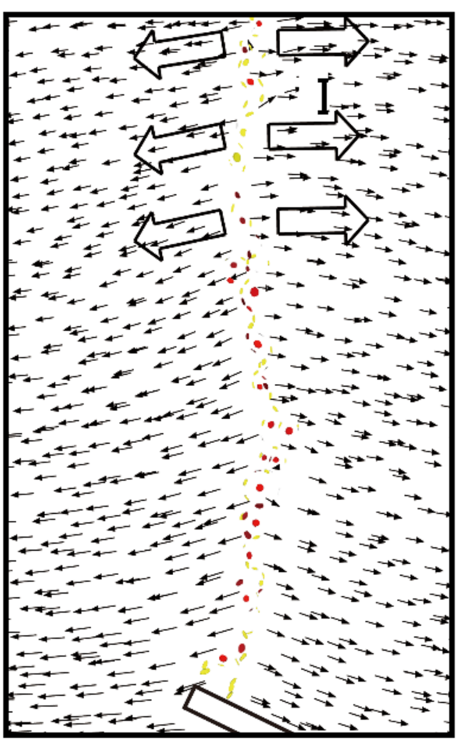

Fig. 11 The particle velocity vector field outside the rock bridge before splitting failure

When σ_i reaches about 65% σ_c, crack 3 initiates from the top of wing crack 1 and propagates toward the lower flaw (Fig. 12d). When the rock bridge fractures, all of the three cracks contain both tensile and shear breakages (Fig. 12e).

Figure 13, which corresponds to Fig. 12a, is the particle velocity vector field inside the rock bridge when crack initiates. The particles on the right side of wing crack 1 move to the interior of the lower flaw along the normal of flaw surface, while particles on the left side move to the left horizontally. The particle velocity vector field coincides with type IV, where the initiation of wing crack 1 is mixed tensile and shear crack. However, wing crack 2 seems to be tensile crack, but there are a small number of shear breakages mixing in tensile breakages.

Figure 14 which corresponds to Fig. 12c is the particle velocity vector field inside the rock bridge during the propagation of wing crack. The center of rock bridge is isolated by wing cracks 1 and 2 as a core. Due to the shear and dragging effects induced by the opposite direction of particle velocity on either side of the rock bridge, the particle velocity vector field of this part evolves into a rotation distribution. Influenced by this, the particle velocity vector fields around wing cracks 1 and 2 coincide with type IV. The propagations of wing cracks 1 and 2 are mix tensile and shear cracks.

Figure 15, which corresponds to Fig. 12d and e, is the particle velocity vector field inside the rock bridge before rock bridge fracture. The initiation of crack 3 disturbs the rotation distribution. The particles between wing cracks 1 and 3 tend to be static (region within the red circle in Fig. 15a). The particle velocity vector field around crack 3 turns to coincide with type III. The wing cracks 1 and 2 remain mixed tensile and shear crack until rock bridge fracture.

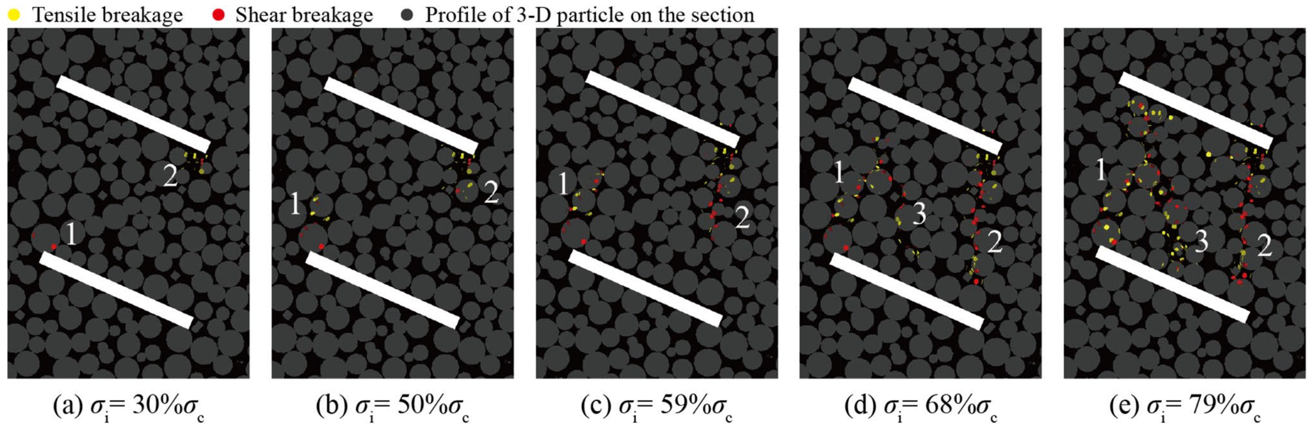

Fig. 12 The types of breakage constituting the wing crack outside the rock bridge in different stresses

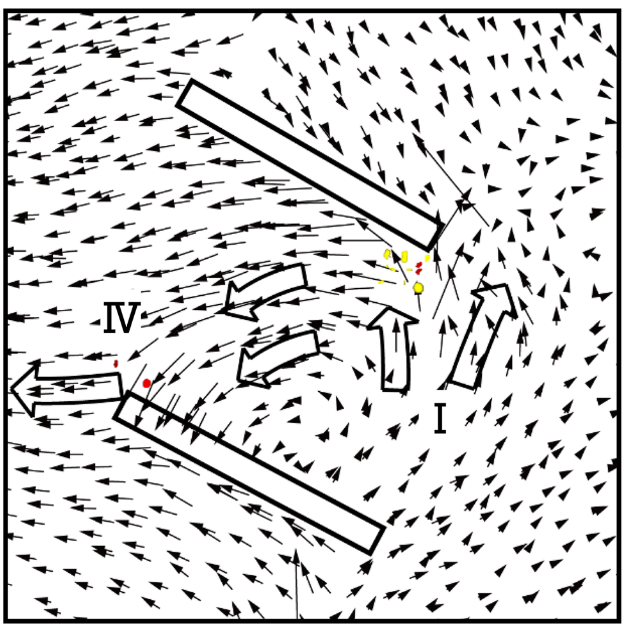

Fig. 13 The particle velocity vector field inside the rock bridge when crack initiation

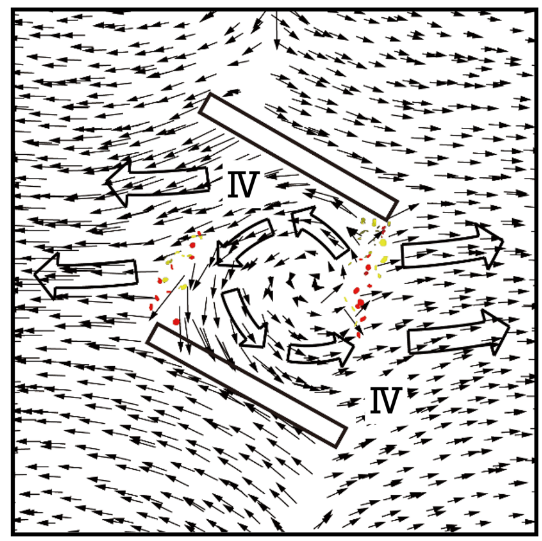

Fig. 14 The particle velocity vector field inside the rock bridge during the propagation of crack

5 The Impacts of Interaction Between 3-D Flaws on Crack Evolution Mechanism

5.1 The Impact on the Initiation Mechanism of Wing Crack

The interaction between flaws changes the initiation mechanism of wing crack. In rock bridge, wing crack 1 initiates as mixed tensile and shear crack while the other wing cracks initiate as tensile cracks. Rock bridge is the region which is the most directly influenced by the interaction between flaws; the particle force and velocity fields are extremely complicated. Besides, the flaw adopted in this research is open flaw. The particles on the flaw surface will deform to the interior space of flaw, which may induce slipping and shear breakage between particles at the flaw tip. The particle velocity vector field in the rock bridge also verifies the rationality of mixed tensile and shear crack.

5.2 The Impact on the Propagation Mechanism of Wing Crack

The interaction between flaws changes the propagation mechanism of wing crack. In the single-flaw condition, when shear breakage stops initiating, wing crack ceases to propagate, while in the double flaws condition, after the formation

Fig. 15 The particle velocity vector field inside the rock bridge before rock bridge fracture

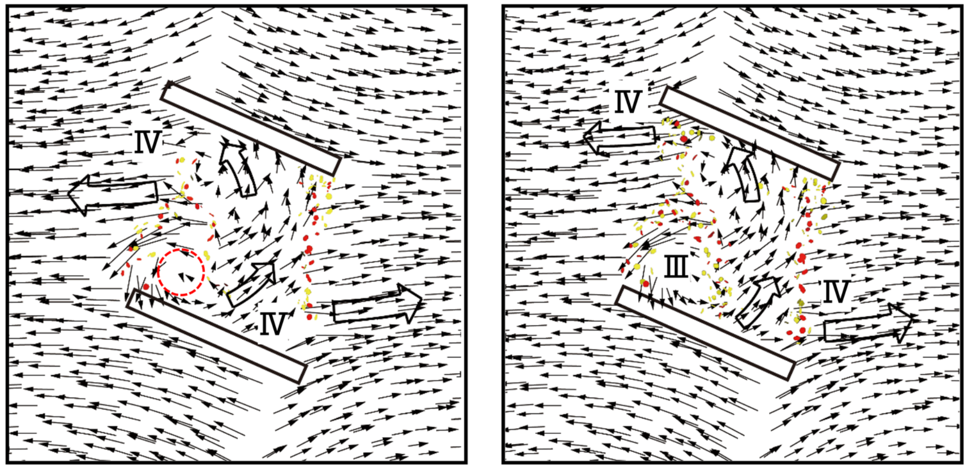

(a) σ_i= 68% σ_c (b) σ_i= 79% σ_c

of the vertical large crack, the shear breakage is basically not initiating but the tensile breakage increases sharply, inducing the splitting failure. These indicate that the shear breakage is the key factor controlling the propagation of wing crack in the single-flaw condition, while in double-flaw condition, this key factor turns into tensile breakage.

The interaction between flaws significantly promotes the generation of tensile breakage. Figure 16 is the comparison of particle velocity between different conditions when wing cracks propagate to approximate length: the red dots numbered in Fig. 16a and b are the monitor points to which the nearest particle is selected to obtain its velocity vector. At this stage, the particle velocity vector field returns to symmetrical distribution, and only tensile effect exists between particles. From Fig. 16c it can be observed that the particle velocity at each monitor point in double-flaw condition is significantly higher than that in the single flaw condition, which indicates that tensile effect is much greater in double-flaw condition. Hence, the wing crack in double-flaw condition can continue to propagate until specimen splitting failure.

5.3 The Impact on the Quantity and Percent of Tensile and Shear Breakages

Figures 17 and 18 are the variations of breakage quantity with axial load and time increasing in different conditions, respectively. The axial load σ_i is normalized by the peak strength σ_c. The left vertical axis is the ratio of σ_i to σ_c, which is expressed as a percentage. The red columns denote

Fig. 16 The comparison of particle velocities between different conditions when wing cracks propagate to an approximate length

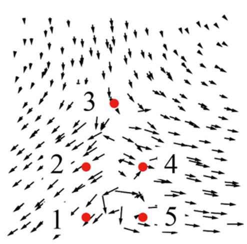

(a) Particle velocity vector field at the top of wing crack in single flaw condition when σ_i=89%σ_c

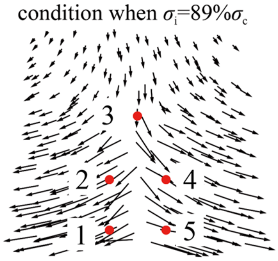

(b) Particle velocity vector field at the top of wing crack in double flaws condition when σ_i=79%σ_c

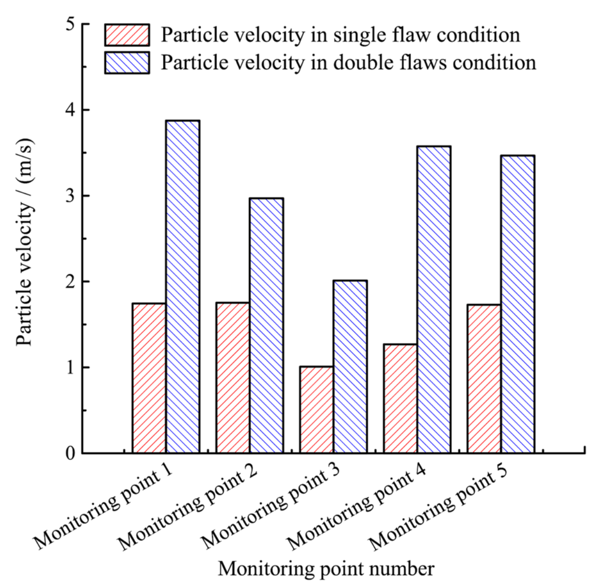

(c) Comparision of particle velocity at each monitoring point between single flaw and double flaws condition

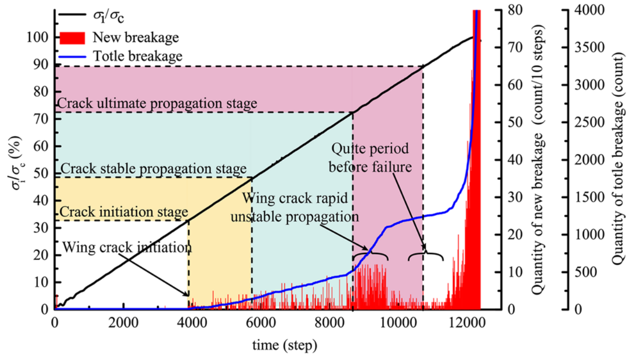

Fig. 17 The variation of breakage quantity with axial load and time increasing in single flaw condition

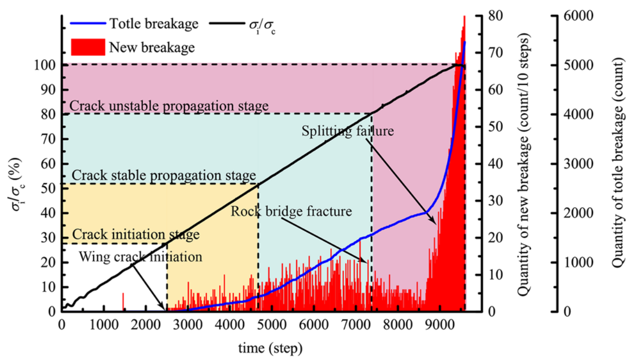

Fig. 18 The variation of breakage quantity with axial load and time increasing in double flaws condition

newly added breakage quantity every ten time steps. The blue curve represents the total breakage quantity.

In single flaw condition, when wing crack initiates, the red column is generated densely and the blue curve rises approximately linearly. After the formation of petal wing crack ($\sigma_i/\sigma_c \approx 72\%$), the red column increases rapidly and the blue curve rises steeply. Afterward, the red column decreases significantly, and wing crack ceases to propagate gradually. The generation of breakage gets into a quiet period before specimen failure, which is similar to the characteristics of the AE signal before rock failure (Spetzler et al. 1987; Wang 2014; Su et al. 2018). When σ_i/σ_c reaches about 95%, the red column increases sharply, and a large number of cracks are generated, inducing specimen burst failure.

In double-flaw condition, the variation of breakage quantity is similar to that in single-flaw condition before the fracture of rock bridge. However, the quiet period does not appear in this condition. When σ_i/σ_c reaches about 95%, the red column increases rapidly and the blue curve rise steeply, which corresponds to the rapid propagation of vertical large crack and the splitting failure.

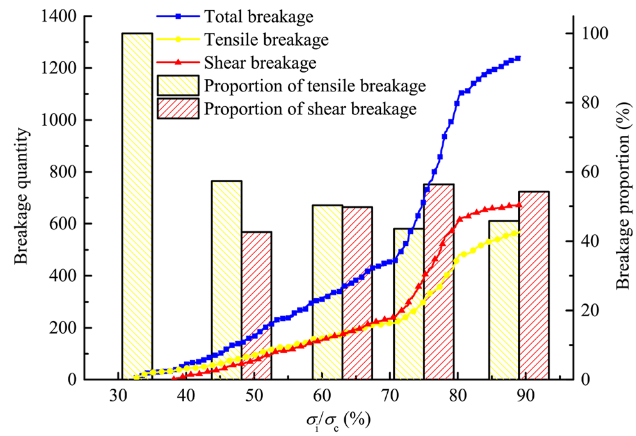

Fig. 19 The proportion variation of tensile and shear breakage with stress increasing in single flaw condition

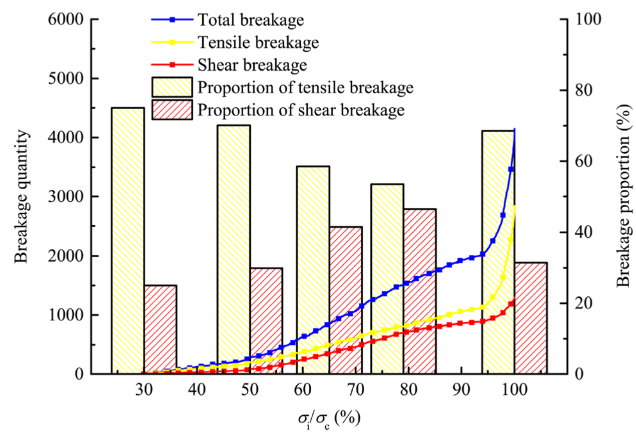

Fig. 20 The variation of tensile and shear breakage quantities with stress increasing in double flaws condition

Figure 19 shows the variation of tensile and shear breakage quantities with stress increasing: the five groups of columns are proportions of tensile and shear breakage corresponding to the five stresses in Fig. 6. When crack initiates, the yellow curve overlaps with the blue curve which indicates the crack is composed of tensile breakages. When $\sigma_i/\sigma_c \approx 38.2\%$, shear breakage begins to initiate. During the stable propagation of wing crack, the quantities of tensile breakage and shear breakage are almost equal. Before wing crack gets into unstable propagation stage, the quantity of shear breakage begins to exceed that of tensile breakage and the proportion can at the highest be 58.7%. When wing crack approaches the ultimate propagation length, the quantity of shear breakage stops increasing basically, and the proportions of tensile and shear breakage are 45.76% and 54.24%, respectively.

Figure 20 shows the variation of tensile and shear breakage quantities: with stress increasing in double-flaw condition, the five groups of columns are the proportions of tensile and shear breakage corresponding to five σ_i/σ_c states (30%, 50%, 65%, 79%, and 100%). Different from the single-flaw condition, the proportion of shear breakage is not zero when crack initiates because the initiation of wing crack 1 inside the rock bridge is mixed tensile and shear crack. Moreover, the quantity of tensile breakage is always more than that of shear breakage. The proportion of tensile breakage can the lowest be 52.86% when σ_i/σ_c equals 83.27%. Then, wing cracks get into unstable propagation, and the quantity of tensile breakage increases rapidly. When the specimen reaches splitting failure, the proportions of tensile and shear breakage are 68.52% and 31.48%, respectively.

Figure 21 shows the comparison of breakage quantities between different conditions during the loading process. In the most stage of loading, the breakage quantity in double-flaw condition is more than that in the single-flaw condition because with the promotion of the interaction between flaws on crack evolution, the extension of wing crack in double-flaw condition is much larger than that in single-flaw condition. However, before specimen failure, the breakage quantity in the single-flaw condition exceeds that in double-flaw condition. It is because that the failure mode in the single flaw condition is burst failure, the fracture surfaces are messy and intricate (Fig. 22a). While the failure mode in double-flaw condition is splitting failure (Fig. 22b), the fracture surface scale is smaller than that in the single flaw condition.

6 Discussion

Compared to the standard BPM, the FJM is more suitable for the 3-D cracking process simulation. This may be due to some unique characteristics of FJM.

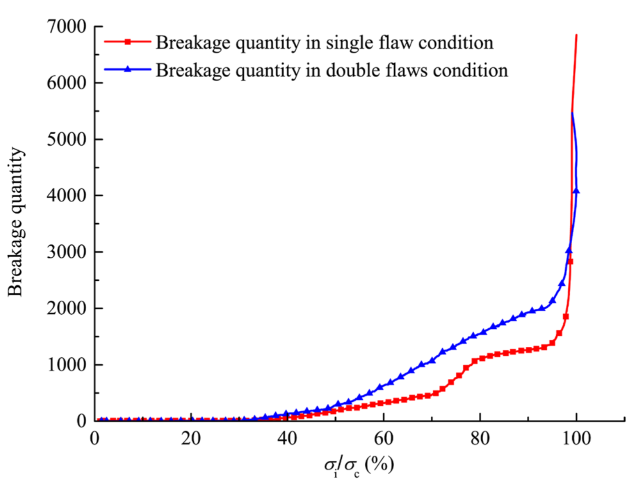

Fig. 21 The comparison of breakage quantity between different conditions

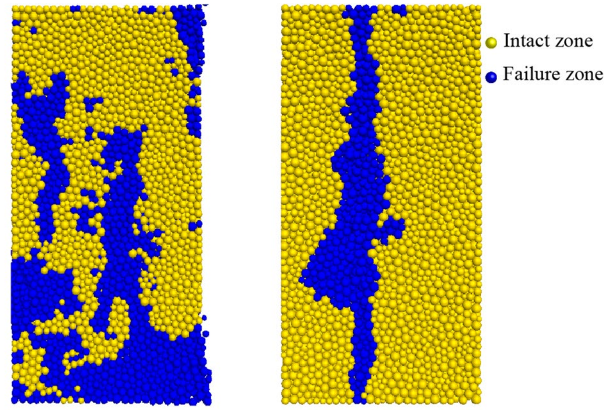

(a) Single flaw condition (b) Double flaws condition

Fig. 22 The specimen failure modes in different conditions

6.1 Particle Interlocking

The FJM is shown in Fig. 4. The effective surface of sphere particle is modified by the notional surface. The particle can be considered as a skirted grain. When the contact breaks, the notional surface still exists. This structure can provide particle interlocking and rotational resistance even after contact damage, while in standard BPM, the particle is spherical and the contact will vanish after breaking which leads to particle excessive rolling.

6.2 Proper Rotational Resistance

Particle rotation and rotational resistance play a significant role in simulations (Plassiard et al. 2009; Wang and Mora 2008). In standard BPM, the bending and twisting moments fully contribute to the maximum tensile and shear stresses according to beam theory, as shown in Eq. (1):

$$\begin{aligned}\sigma_{\max} &= \frac{-F_n}{A} + \frac{|M_b|}{I}\bar{R} \\ \tau_{\max} &= \frac{-F_s}{A} + \frac{|M_t|}{J}\bar{R},\end{aligned} \tag{1}$$

where F_n and F_s are the normal and shear forces in the bond, M_b and M_t are the bending and twisting moments acting at the bond center; A, I, and J are the area, inertia moment, and polar inertia moment of the bond cross-section, respectively, and $\bar{R}$ is the average radius of particles in the bond.

However, the full contribution of moments to the maximum stresses leads to low brittleness of the model, according to previous studies (Potyondy 2012b; Ding and Zhang 2014), the moment contributions to the stresses are very small and can be neglected. In FJM, the maximum normal stress and shear stress are given by:

$$\sigma_{\max} = \frac{-F_{\mathrm{n}}}{A}$$
$$\tau_{\max} = \frac{-F_{\mathrm{s}}}{A}. \quad (2)$$

The contribution of moments to the maximum normal and shear stresses is completely eliminated. But the model can still provide rotational resistance due to its special structure, as mentioned in Sect. 6.1.

7 Conclusion

In this research, the crack evolution modes of 3-D flaws are summarized by laboratory experiment and numerical simulation. The microscopic mechanisms of crack evolution are analyzed and the impacts of interaction between flaws on crack evolution are investigated.

The simulation results are in good agreement with the experimental results, which indicates that the flat-joint contact model based on PFC3D is appropriate to model the cracking process of 3-D flaw in brittle material.

The method of particle velocity trend lines is introduced to analyze the mechanism of crack evolution. Four types of particle velocity vector fields corresponding to typical cracks are proposed. Type I and III represent tensile crack, type II and IV represent mixed tensile and shear crack.

The initiation of wing crack is generally tensile crack, but it may turn into mixed tensile and shear crack in rock bridge. The interaction between flaws and the structure of the open flaw are important reasons for this transition.

The propagation of wing crack is mixed tensile and shear crack, but the roles of tensile and shear breakage in wing crack propagation vary for different conditions. In the single-flaw condition, shear breakage is the key factor that controls the further propagation of wing crack, while in double flaws condition, this key factor turns into tensile breakage.

The interaction between flaws has an important impact on the specimen failure mode. In the single-flaw condition, the propagation of wing crack is insufficient to cause specimen failure directly and the failure mode is burst failure. But in double-flaw condition, the "self-limiting" effect is effectively overcome by the interaction between flaws, which promotes wing crack to propagate continually and induces specimen splitting failure.

Acknowledgements The research reported in this paper was financially supported by the National Natural Science Foundation of China (Grant nos. 51579140, 51509146, 41877239, 51422904, and 51879149), and the Shandong Provincial Natural Science Foundation (No. JQ201513), and Free Exploration Foundation of Qilu School of Transportation, Shandong University, P.R.China (Grant no. 2019B47_1).

Authors Contributions All authors contributed to the study conception and design. Supervision and project administration were performed by SY. Material preparation, data collection and analysis were performed by BL. The first draft of the manuscript was written by BL. Simulation method and software code were provided by WC. Funding acquisition was provided by SY, WZ, LY, YX and YL. All authors commented on previous versions of the manuscript. All authors read and approved the final manuscript.

Compliance with Ethical Standards

Conflict of interest The authors declare no conflict of interest.

References

Adams M, Sines G (1978) Crack extension from flaws in a brittle material subjected to compression. Tectonophysics 49:97–118. https://doi.org/10.1016/0040-1951(78)90099-9

Bahaaddini M, Sheikhpourkhani AM, Mansouri H (2019) Flat-joint model to reproduce the mechanical behaviour of intact rocks. Eur J Environ Civ Eng. https://doi.org/10.1080/19648189.2019.1579759

Bobet A (2000) The initiation of secondary cracks in compression. Eng Fract Mech 66:187–219. https://doi.org/10.1016/S0013-7944(00)00009-6

Bobet A, Einstein HH (1998a) Fracture coalescence in rock-type materials under uniaxial and biaxial compression. Int J Rock Mech Min Sci 35:863–888. https://doi.org/10.1016/S0148-9062(98)00005-9

Bobet A, Einstein HH (1998b) Numerical modeling of fracture coalescence in a model rock material. Int J Fract 92:221. https://doi.org/10.1023/A:1007460316400

Bocca P, Carpinteri A, Valente S (1990) Size effects in the mixed mode crack propagation: softening and snap-back analysis. Eng Fract Mech 35:159–170. https://doi.org/10.1016/0013-7944(90)90193-K

Bubeck A, Walker RJ, Healy D, Dobbs M, Holwell DA (2017) Pore geometry as a control on rock strength. Earth Planet Sci Lett 457:38–48. https://doi.org/10.1016/j.epsl.2016.09.050

Budyn E, Zi G, Moes N, Belytschko T (2004) A model for multiple crack growth in brittle materials without remeshing. Int J Numer Methods Eng 61:1741–1770. https://doi.org/10.1002/nme.1130

Cao P, Liu T, Pu C, Lin H (2015) Crack propagation and coalescence of brittle rock-like specimens with pre-existing cracks in compression. Eng Geol 187:113–121. https://doi.org/10.1016/j.enggeo.2014.12.010

Cao R-H, Cao P, Lin H, Pu C-Z, Ou K (2016) Mechanical behavior of brittle rock-like specimens with pre-existing fissures under uniaxial loading: experimental studies and particle mechanics approach. Rock Mech Rock Eng 49:763–783. https://doi.org/10.1007/s00603-015-0779-x

Cheng H, Zhou X, Zhu J, Qian Q (2016) The effects of crack openings on crack initiation, propagation and coalescence behavior in rock-like materials under uniaxial compression. Rock Mech Rock Eng 49:3481–3494. https://doi.org/10.1007/s00603-016-0998-9

Ding X, Zhang L (2014) A new contact model to improve the simulated ratio of unconfined compressive strength to tensile strength in bonded particle models. Int J Rock Mech Min Sci 69:111–119. https://doi.org/10.1016/j.ijrmms.2014.03.008

Dyskin A et al (1994a) Study of 3-D mechanisms of crack growth and interaction in uniaxial compression. ISRM News J 2:17–20

Dyskin AV, Jewell RJ, Joer H, Sahouryeh E, Ustinov KB (1994b) Experiments on 3-D crack growth in uniaxial compression. Int J Fract 65:R77–R83. https://doi.org/10.1007/bf00012382

Dyskin AV, Sahouryeh E, Jewell RJ, Joer H, Ustinov KB (2003) Influence of shape and locations of initial 3-D cracks on their growth in uniaxial compression. Eng Fract Mech 70:2115–2136. https://doi.org/10.1016/S0013-7944(02)00240-0

Fu J, Zhu W, Xie F, Xue W, Zhang D, Li Y (2013) Experimental studies and elasto-brittle simulation of propagation and coalescence process of two three-dimensional flaws in rocks. Rock Soil Mech 34:2489–2495. https://doi.org/10.16285/j.rsm.2013.09.013

Germanovich LN, Dyskin AV (2000) Fracture mechanisms and instability of openings in compression. Int J Rock Mech Min Sci 37:263–284. https://doi.org/10.1016/S1365-1609(99)00105-7

Ghazvinian A, Sarfarazi V, Schubert W, Blumel M (2012) A study of the failure mechanism of planar non-persistent open joints using PFC2D. Rock Mech Rock Eng 45:677–693. https://doi.org/10.1007/s00603-012-0233-2

Hosseini-Tehrani P, Hosseini-Godarzi AR, Tavangar M (2005) Boundary element analysis of stress intensity factor KI in some two-dimensional dynamic thermoelastic problems. Eng Anal Bound Elem 29:232–240. https://doi.org/10.1016/j.enganabound.2004.12.009

Lee H, Jeon S (2011) An experimental and numerical study of fracture coalescence in pre-cracked specimens under uniaxial compression. Int J Solids Struct 48:979–999. https://doi.org/10.1016/j.ijsolstr.2010.12.001

Li B, Zhu W, Yang L, Yu S, Mei J, Cai W (2019) Experimental research on propagation mode of 3D hollow crack and material failure strength under hydro-mechanical coupling. J Cent South Univ (Sci Technol) 50:1192–1202. https://doi.org/10.11817/j.issn.1672-7207.2019.05.023

Lu X, Wu W-L (2006) A subregion DRBEM formulation for the dynamic analysis of two-dimensional cracks. Math Comput Model 43:76–88. https://doi.org/10.1016/j.mcm.2005.03.009

Manouchehrian A, Marji MF (2012) Numerical analysis of confinement effect on crack propagation mechanism from a flaw in a pre-cracked rock under compression. Acta Mech Sin 28:1389–1397. https://doi.org/10.1007/s10409-012-0145-0

Manouchehrian A, Sharifzadeh M, Marji MF, Gholamnejad J (2014) A bonded particle model for analysis of the flaw orientation effect on crack propagation mechanism in brittle materials under compression. Arch Civ Mech Eng 14:40–52. https://doi.org/10.1016/j.acme.2013.05.008

Park CH, Bobet A (2010) Crack initiation, propagation and coalescence from frictional flaws in uniaxial compression. Eng Fract Mech 77:2727–2748. https://doi.org/10.1016/j.engfracmech.2010.06.027

Plassiard J-P, Belheine N, Donzé F-V (2009) A spherical discrete element model: calibration procedure and incremental response. Granul Matter 11:293–306. https://doi.org/10.1007/s10035-009-0130-x

Potyondy D (2012a) PFC 2D flat joint contact model. Itasca Consulting Group Inc., Minneapolis

Potyondy D (2012b) A flat-jointed bonded-particle material for hard rock. In: Paper presented at the 46th US rock mechanics/geomechanics symposium 2012, Chicago, IL, USA, 24–27 June

Potyondy D (2013) PFC3D flat joint contact model version 1. Itasca Consulting Group, Minneapolis

Potyondy D, Cundall PA (1996) Modeling rock using bonded assemblies of circular particles. In: Paper presented at the 2nd North American rock mechanics symposium, Montreal, Quebec, Canada

Potyondy DO, Cundall PA (2004) A bonded-particle model for rock. Int J Rock Mech Min Sci 41:1329–1364. https://doi.org/10.1016/j.ijrmms.2004.09.011

Sahouryeh E, Dyskin AV, Germanovich LN (2002) Crack growth under biaxial compression. Eng Fract Mech 69:2187–2198. https://doi.org/10.1016/S0013-7944(02)00015-2

Sarfarazi V, Ghazvinian A, Schubert W, Blumel M, Nejati HR (2014) Numerical simulation of the process of fracture of echelon rock joints. Rock Mech Rock Eng 47:1355–1371. https://doi.org/10.1007/s00603-013-0450-3

Shen B, Stephansson O, Einstein HH, Ghahreman B (1995) Coalescence of fractures under shear stresses in experiments. J Geophys Res Solid Earth 100:5975–5990. https://doi.org/10.1029/95jb00040

Spetzler H, Sondergeld C, Sobolev G, Salov B (1987) Seismic and strain studies on large laboratory rock samples being stressed to failure. Tectonophysics 144:55–68. https://doi.org/10.1016/0040-1951(87)90008-4

Su G, Shi Y, Feng X, Jiang J, Zhang J, Jiang Q (2018) True-triaxial experimental study of the evolutionary features of the acoustic emissions and sounds of rockburst processes. Rock Mech Rock Eng 51:375–389. https://doi.org/10.1007/s00603-017-1344-6

Wang C-l (2014) Identification of early-warning key point for rockmass instability using acoustic emission/microseismic activity monitoring. Int J Rock Mech Min Sci 71:171–175. https://doi.org/10.1016/j.ijrmms.2014.06.009

Wang Y, Mora P (2008) Modeling wing crack extension: implications for the ingredients of discrete element model. Pure Appl Geophys 165:609–620. https://doi.org/10.1007/s00024-008-0315-y

Wang H, Dyskin A, Pasternak E, Dight P, Sarmadivaleh M (2019) Experimental and numerical study into 3D crack growth from a spherical pore in biaxial compression. Rock Mech Rock Eng. https://doi.org/10.1007/s00603-019-01899-1

Wong RHC, Chau KT (1998) Crack coalescence in a rock-like material containing two cracks. Int J Rock Mech Min Sci 35:147–164. https://doi.org/10.1016/S0148-9062(97)00303-3

Wong RHC, Huang ML, Jiao MR, Tang CA, Zhu WS (2004a) The mechanisms of crack propagation from surface 3-D fracture under uniaxial compression. Key Eng Mater 261–263:219–224. https://doi.org/10.4028/www.scientific.net/KEM.261-263.219

Wong RHC, Law CM, Chau KT, Zhu W-S (2004b) Crack propagation from 3-D surface fractures in PMMA and marble specimens under uniaxial compression. Int J Rock Mech Min Sci 41:37–42. https://doi.org/10.1016/j.ijrmms.2004.03.016

Wong RHC, Guo YSH, Li LY, Chau KT, Zhu WS, Li SC (2006) Anti-wing crack growth from surface flaw in real rock under uniaxial compression. In: Gdoutos EE (ed) Fracture of nano and engineering materials and structures. Springer, Dordrecht, pp 825–826

Wong RHC, Guo YSH, Chau KT, Zhu W, Li S (2007) The crack growth mechanism from 3-D surface flaw with strain and acoustic emission measurement under axial compression. Key Eng Mater KEY ENG MAT 353–358:2357–2360. https://doi.org/10.4028/www.scientific.net/KEM.353-358.2357

Wu S, Xu X (2016) A study of three intrinsic problems of the classic discrete element method using flat-joint model. Rock Mech Rock Eng 49:1813–1830. https://doi.org/10.1007/s00603-015-0890-z

Xu C, Fowell RJ (1994) Stress intensity factor evaluation for cracked chevron notched brazilian disc specimens. Int Rock Mech Min Sci Geomech Abstr 31:157–162. https://doi.org/10.1016/0148-9062(94)92806-1

Xu X, Wu S, Gao Y, Xu M (2016) Effects of micro-structure and micro-parameters on Brazilian tensile strength using flat-joint model. Rock Mech Rock Eng 49:3575–3595. https://doi.org/10.1007/s00603-016-1021-1

Yang S-Q, Huang Y-H (2018) Failure behaviour of rock-like materials containing two pre-existing unparallel flaws: an insight from particle flow modeling. Eur J Environ Civ Eng 22:s57–s78. https://doi.org/10.1080/19648189.2017.1366954

Yang S-Q, Jing H-W (2010) Strength failure and crack coalescence behavior of brittle sandstone samples containing a single fissure under uniaxial compression. Int J Fract 168:227–250. https://doi.org/10.1007/s10704-010-9576-4

Yang X-X, Qiao W-G (2018) Numerical investigation of the shear behavior of granite materials containing discontinuous joints by utilizing the flat-joint model. Comput Geotech 104:69–80. https://doi.org/10.1016/j.compgeo.2018.08.014

Yang S-Q, Huang Y-H, Jing H-W, Liu X-R (2014) Discrete element modeling on fracture coalescence behavior of red sandstone containing two unparallel fissures under uniaxial compression. Eng Geol 178:28–48. https://doi.org/10.1016/j.enggeo.2014.06.005

Yin P, Wong RHC, Chau KT (2014) Coalescence of two parallel pre-existing surface cracks in granite. Int J Rock Mech Min Sci 68:66–84. https://doi.org/10.1016/j.ijrmms.2014.02.011

Zhang X-P, Wong LNY (2012) Cracking processes in rock-like material containing a single flaw under uniaxial compression: a numerical study based on parallel bonded-particle model approach. Rock Mech Rock Eng 45:711–737. https://doi.org/10.1007/s00603-011-0176-z

Zhang X-P, Wong LNY (2013) Crack initiation, propagation and coalescence in rock-like material containing two flaws: a numerical study based on bonded-particle model approach. Rock Mech Rock Eng 46:1001–1021. https://doi.org/10.1007/s00603-012-0323-1

Zhang X-P, Wong LNY (2014) Displacement field analysis for cracking processes in bonded-particle model. Bull Eng Geol Env 73:13–21. https://doi.org/10.1007/s10064-013-0496-1

Zhang X-P, Liu Q, Wu S, Tang X (2015) Crack coalescence between two non-parallel flaws in rock-like material under uniaxial compression. Eng Geol 199:74–90. https://doi.org/10.1016/j.enggeo.2015.10.007

Zhou X, Yang H, Dong J (2010) Numerical simulation of multiple-crack growth under compressive loads. Chin J Geotech Eng 32:192–197 (in Chinese with English abstract)

Zhou X-P, Zhang J-Z, Wong LNY (2018) Experimental study on the growth, coalescence and wrapping behaviors of 3D cross-embedded flaws under uniaxial compression. Rock Mech Rock Eng 51:1379–1400. https://doi.org/10.1007/s00603-018-1406-4

Zhuang X, Chun J, Zhu H (2014) A comparative study on unfilled and filled crack propagation for rock-like brittle material. Theoret Appl Fract Mech 72:110–120. https://doi.org/10.1016/j.tafmec.2014.04.004